AFRC 2024 Industrial Combustion Symposium
Calgary, Alberta Canada
September 30 – October 3, 2024

Experimentally Validated Data Analytics Method for Gas Flare Combustion Efficiency Monitoring

Nicholas Rock[1], Keith D. Rein
Spectral Energies, LLC, Beavercreek, OH, 45430, USA

Aaron Naidu, Nicklaus M. Schoenfuss, David Wu, Benjamin Emersion
Georgia Institute of Technology, Atlanta, GA, 30318, USA

The notable increase in the global average surface temperature relative to pre-industrial levels has motivated enhanced efforts to reduce greenhouse gas emissions. Although emissions of both carbon dioxide and methane have contributed to the problem, emissions of methane are especially concerning due to their much larger global warming potential. Therefore, companies generally take steps to avoid the unrestrained release of methane into the atmosphere. Natural gas flaring is one of these mitigating practices and involves burning excess natural gas that must be disposed of for economic, safety, or operational reasons. However, gas flares often operate with low combustion efficiency and unburned methane is nonetheless vented to the atmosphere as a result. Furthermore, in the event that flameout occurs, exorbitant methane emissions will ensue and defeat the purpose of the gas flare altogether. This study presents a data analytics methodology for detecting precursors to flameout in natural gas flares. It involves first filtering the data with a time series model and then identifying statistical irregularities using a fault detection algorithm. The data analytics method was applied to quantitative temperature and acoustics measurements that were taken in an industry relevant gas flare test rig. Specifically, (4) 20 kHz microphones and H_2O absorption spectroscopy data acquired at 1 kHz were used to monitor the flare rig's combustion process. These data provided a clear indication of flameout. Furthermore, the data analytics method identified local extinction processes prior to the occurrence of flameout, which are the underlying physical phenomena behind incomplete combustion. These local extinction processes increased in frequency as flameout was approached. On the other hand, the data analytics method did not detect irregular combustion processes in the data for stable burning flames. These results have implications for gas flare monitoring as the feedback from the data analytics method would help ensure that methane emissions from either flameout or incomplete combustion are avoided.

I. Nomenclature

a_i = Residuals from the ARIMA model
b = Rational subgroup size
ARIMA = Autoregressive Integrated Moving Average
DOE = Department of Energy
EPA = Environmental Protection Agency
EWRMS = Exponentially Weighted Root Mean Squared-error
FO = Flameout
HEI = High Energy Ignition
GWP = Global Warming Potential

---

[1] Corresponding Author Email: nicholas.rock@spectralenergies.com

$IGARCH$ = Integrated Generalized Autoregressive Conditional Heteroscedasticity
OGI = Optical gas imaging
T_n = Total number of samples in a time series
$\dot{V}_{CH4}$ = Volume flow rate of methane

Z_i = Array of curated test data
α_0 = Constant in the IGARCH model
α_1 = Coefficient in the IGARCH model
β = Predetermined false alarm rate
γ = Constant governing the amount of weight placed on the memory of S_k
η_1 = Coefficient in the IGARCH model
θ_1 = Coefficient in the ARIMA model
μ = Mean of ∇X_i values
σ_i^2 = Conditional variance
ϕ_1 = Coefficient in the ARIMA model
ϕ_2 = Coefficient in the ARIMA model

∇X_i = Difference in the absorption temperature data at consecutive sampling intervals

II. Introduction

Significant reductions in greenhouse gas (GHG) emissions are required in order to prevent a 2–11.5 °F increase in the global average temperature by the year 2100 [1]. Without effective interventions, deleterious ecological effects such as forest fires, droughts, heat waves, diminished forest populations, and a substantial rise in the average sea level can be expected to occur. Although emissions of both carbon dioxide and methane have contributed to this changing state of the global climate, emissions of methane are especially concerning due to their much larger global warming potential (GWP). Methane has a GWP that is 73 times greater than CO_2 over a 20 year period and 28 times greater over a 100 year period [2]. Unlike CO_2, methane is not a product of stoichiometric combustion reactions and therefore emissions of methane from combustion systems are largely preventable. Since methane experiences its largest global warming potential shortly after it is emitted into the atmosphere, reducing methane emissions is often regarded as the fastest way to immediately mitigate the advancement of climate change.

Petrochemical plants, refineries, and many other industries commonly use gas flaring as a mitigating practice to avoid the unrestrained release of methane into the atmosphere. However, gas flares often operate with low combustion efficiency and unburned methane is nonetheless vented to the atmosphere as a result. Furthermore, in the event that flameout (FO) occurs, exorbitant methane emissions will ensue and defeat the purpose of the gas flare altogether. The United States' Environmental Protection Agency (EPA) recognizes the potential for gas flares to emit unburned methane at dangerously high levels. Therefore, On December 2, 2023, the EPA issued the Controlling Air Pollution from Oil and Natural Gas Operations Ruling [3], which has significant implications for the future of flaring in the United States. Specifically, the rule bans routine flaring of natural gas at the sites of new oil wells and mandates regular monitoring of existing flares. Furthermore, states are required to submit methane reduction plans within two years of the ruling and compliance is required during the subsequent three years. The flare monitoring requirements in the EPA's rule will involve monthly inspections of existing gas flares for 95% combustion efficiency, continuous burning of the pilot flame(s), and the absence of visible emissions. A significant element of the EPA's December 2023 rule is that it encourages the development of alternative technologies for flare monitoring. Users of existing flares are given the option to replace the standard methane detection method (i.e., optical gas imaging cameras) with an alternative method that consistently achieves 95% combustion efficiency [3]. This ruling signals a move towards reduced flaring practices and motivates advanced monitoring technologies in defense of the flaring industry. Therefore, technologies are needed that can quickly detect a decrease in combustion efficiency and then modify the operation of a gas flare to prevent further methane emissions.

In order to accomplish the EPA's climate goals, effective flare monitoring technologies must also include the ability to accurately detect flameout. Unfortunately, this capability is often lacking in practice as a recent study [4] indicated that 5% of all flares in Texas' Permian Basin were actually operating unlit. In a review article summarizing the extensive literature on premixed bluff-body stabilized flames, Shanbhogue et al. [5] describe flameout (FO) as the culmination of a series of localized extinction and unstable fluid mechanic processes that ultimately lead to the complete loss of the flame. It is these precursors to flameout that decrease a flame's combustion efficiency. In a key study that shaped this phenomenological model, Nair and Lieuwen [6] observed instances of local flame extinction that were linked to the instantaneous flame stretch rate exceeding the extinction stretch rate. However, they found that the flame and flow topology generally maintained the same shape and structure as it did during stable burning. With further reductions in the equivalence ratio, these localized extinction processes became more common until the previously symmetric flow field underlying Nair and Lieuwen's [6] bluff-body stabilized flame intermittently experienced large-scale alterations that greatly distorted the flame. Multiple researchers have since verified this flow field transition [5] and provided mechanistic explanations [7], [8] for its occurrence. Localized flame extinction grows rapidly in this state and complete flameout transpires shortly thereafter.

Elevated gas flares, where natural gas is transported through a tower and burned as an unconfined, nonpremixed flame, are the most common flaring configuration. This approach typically includes one or more pilot flames located at the gas flare's tip. These pilot flames provide a continuous ignition source that helps stabilize the nonpremixed flame against adverse conditions, such as high winds, extremely high or low fuel flow rates relative to the flow of available oxidizer, or over dilution by steam or air. Although many of the previously discussed flame stability concepts are applicable to elevated gas flares, the need to rapidly mix fuel and air introduces added complexity and significant differences in near-flameout behavior. For instance, nonpremixed flames lift off the burner outlet as flameout is approached, whereas upstream propagating extinction processes cause the burner outlet to be where bluff-body stabilized premixed flames are last observed prior to flameout. Furthermore, there are unique mechanisms by which nonpremixed flames can locally extinguish and re-ignite. These include local extinction by excessive scalar dissipation rates [9] and re-ignition through advecting flame kernels [10] or propagating edge flames [11].

Flame monitoring and flameout forecasting have historically been conducted by applying heuristic methods to kHz rate chemiluminescence and/or acoustic data. One of the most commonly used approaches is Thiruchengode's [12] double threshold method, which identifies extinction processes as instances where the time series data descends below and then recovers above two thresholds. These thresholds are essentially a percentage of either the local mean or root mean square of the data that are determined using several established criteria [13]. Other techniques involve monitoring various statistical features of the data relative to a threshold. For example, Yi and Gutmark [14] tracked the normalized root mean squared error of filtered chemiluminescence data. Alternatively, Unni and Sujith [15] used the rate of recurrence, which is the proportion of pairs of data points whose distance is greater than some threshold, to assess their combustor's performance from acoustic data. Mondal et al. [16] developed a hidden Markov model approach that avoids the arbitrariness that exists with threshold-based methods. However, their method relies instead on phenomenological insights that are specific to certain operating conditions in their particular combustor geometry.

This study presents a statistically rigorous method for detecting precursors to flameout in natural gas flares. It is based on a data analytics methodology that was developed by Peters et al. [17] and originally applied to data from swirl-stabilized spray flames. In the current work, the data analytics method was applied to quantitative temperature and acoustics measurements that were taken in an industry relevant gas flare test rig. It involved first filtering these data with a time series model and then identifying statistical irregularities, or "alarms", using a fault detection algorithm. These alarms can then be used to make appropriate modifications to the operation of a gas flare such that the combustion efficiency is increased and unburned methane emissions are avoided.

III. Experimental Setup

Gas Flare Test Rig

The experimental data in this study was acquired from a Zeeco UFAA-4 Air-Assisted Flare Tip Assembly with a 800-000-0049 HSLF-Z-HEI Flare Pilot Assembly. This 4 inch diameter air-assisted gas flare, which shown in Figure 1, included a continuously burning pilot flame, flame stabilization tabs, and dilution air jets for smokeless burning. The gas flare tip was rigidly mounted to an I-beam that kept the flare fixed during operation. The I-beam was welded to a steel pallet that served as the foundation for the test rig.

Air-assisted flares are often preferred by end users because they produce smokeless flames. 22 g/s of assist air was therefore supplied to the test rig by a diesel-fueled Atlas Copco XAS 400 JD portable air compressor. The air mass flow rate was measured using a Coriolis meter. The assist air was injected through 7 air jets that were located around the periphery of the flare's burner tube. All fuel-air mixing happened downstream of the burner tube outlet where the air assist jets impinge on the fuel jet from the main burner tube and stimulate mixing with themselves and the ambient air. Compressed methane cylinders were the fuel source for the gas flare test rig. A three-cylinder manifold supplied the main fuel to the flare, and the pilot flame was fueled by a separate compressed methane cylinder. An Alicat mass flow controller with a 1500 SLPM maximum capacity controlled the fuel flow from the three-cylinder manifold. The main flow of methane ranged between 180-350 SLPM across the studied operating conditions, and the pilot methane pressure was held constant at 50 psi. An electrical box housed a Zeeco High Energy Ignition (HEI) module. The HEI module acted as the ignition source for the experiments by repeatedly discharging 2J sparks to the pilot. Once the pilot flame ignited, the HEI module was disabled and the spark discharge stopped. Fuel flow through the main tube then commenced and was ignited by the pilot flame. The flame exhibited a bright orange color at this stage. Lastly, the assist air was delivered to the flare and the flame achieved the intended smokeless burning mode of operation.

The gas flare experiments were conducted in a controlled manner that provided appropriate training and test data for the data analytics method. This involved acquiring acoustic data and absorption spectroscopy measurements at 5 operating conditions with varying combustion efficiencies: $\dot{V}_{CH4}$=180 SLPM, $\dot{V}_{CH4}$=200 SLPM, $\dot{V}_{CH4}$=250 SLPM, $\dot{V}_{CH4}$=300 SLPM, and $\dot{V}_{CH4}$=350 SLPM. The operating conditions were selected such that the flame gradually progressed from a stable burning condition toward FO, as outlined below:

1. Stable burning condition ($\dot{V}_{CH4}$=350 SLPM) – according to accepted industry standards, a stable burning flame is expected to have 98% combustion efficiency. Since a stable flame could presumably burn indefinitely without experiencing FO, these data were used to train the data analytics method.
2. Intermediate conditions ($\dot{V}_{CH4}$=200, 250, 300 SLPM) – the fuel flow rate was progressively reduced in stepwise increments for each condition between stable burning and FO. The combustion efficiency will begin to decrease in this regime and continue decreasing monotonically the nearer the flame gets to FO.
3. Near FO condition ($\dot{V}_{CH4}$=180 SLPM) – any minor reduction in the fuel flow rate will likely cause FO at this near-limit operating condition. The flame burns here with a low combustion efficiency relative to the stable burning case, and unburned methane emissions are expected in the flame's exhaust. These measurements served as test data for the data analytics method.

Figure 1: Picture of the Georgia Tech gas flare test rig. The air-assisted flare tip was manufactured by Zeeco.

The experiment was repeated ten times for each of the previously described operating conditions. 30 seconds of data were acquired for each test case. An additional test case was also acquired that pushed the gas flare test rig to its operational limit (i.e., $\dot{V}_{CH4}$<180 SLPM). The FO process occurred during this test case and 100 seconds of data were recorded that captured the transient effects associated with this phenomenon. All experiments were performed outdoors at Georgia Tech to include the environmental factors that affect real world flare systems. A Davis Instruments Vantage Vue local weather station operated on site with the flare to accurately measure the ambient weather conditions during the experiments. Differences in ambient conditions between the test cases were relatively minor and they are not believed to have influenced the results of this study.

Optical Gas Imaging (OGI)

OGI cameras were specified as the tool of choice for monitoring methane emissions at flare sites in the EPA's December 2023 rule [3]. The FLIR GFx320 is an EPA certified OGI camera model that was used in this study for the dual-purpose of imaging the flame and detecting unburned methane in the exhaust plume. The FLIR GFx320 is a cooled camera model that is designed to detect methane in the 3.3-3.4 μm absorption band. The internal cooling features of the GFx320 allow it to detect methane leaks at rates as low as 0.6 g/hour. OGI camera images were acquired at 15 Hz throughout the duration of each experimental test case using the camera's high sensitivity mode.

The underlying principle of OGI cameras is that methane absorbs IR radiation over a specific wavelength range (i.e., 3.3-3.4 μm). By spectrally filtering the camera to only detect IR radiation over a specific wavelength range, the camera can detect a contrast between methane, which does absorb the background radiation, and the remaining gas that does not. Unfortunately, hot combustion products create a high degree of ambiguity surrounding the interpretation of OGI camera images from flares. This happens because hot combustion products create sharp changes in the index of refraction of the imaged gas that interfere with the operating principles of the camera. As will be discussed in greater detail below, this interference made identifying both unburned methane emissions and flameout difficult.

PCB Microphones

Unsteady gas expansion [18] associated with the heat release process from combustion causes turbulent flames to radiate sound in all directions. Turbulent flames can therefore be considered an acoustic monopole with an amplitude that is proportional to the heat release rate integrated across the entire flame volume. This study's approach relied heavily on acoustic measurements because they effectively measure the combustion process throughout the entire flame and avoid the field of view issues that accompany light-based sensors. Furthermore, changes in a flame's heat release as FO is approached will consequently alter the acoustic radiation from the flame and allow the combustion efficiency to be qualitatively assessed. The acoustic data were acquired using (4) PCB microphones (see Figure 2) that were located around the flame and sampled at 20 kHz.

Tunable Diode Laser Absorption Spectroscopy (TDLAS)

In addition to the microphone data, temperature measurements were simultaneously acquired in the flame at a height of 4 inches above the flare tip (see Figure 2). These quantitative, path-integrated temperature measurements were performed using tunable diode laser absorption spectroscopy (TDLAS). This technique relies on the principle of quantum mechanics that certain gases absorb radiation at specific wavelengths in a temperature dependent manner. TDLAS measures the amount of intensity that is absorbed as a laser beam passes through a test gas. This absorption measurement is repeated across a relevant wavelength range as the wavelength of the laser is swept. A Thorlabs SL131050-SP1 MEMS-tunable vertical cavity surface emitting laser (VCSEL) was used in this study to measure the temperature of H_2O molecules by sweeping across the wavelength range 1330-1365 nm. These temperature measurements were acquired at 1 kHz across a 9.5 inch beam length. The measurement height above the flare tip was chosen for two reasons. First, this location was near the pilot flame and was therefore critical for flame stabilization. Second, the OGI camera imaging indicated that the flame always occupied this position regardless of the crosswind velocity.

Figure 2: Setup of sensors for acoustic and absorption spectroscopy measurements in the Georgia Tech gas flare test rig.

The gas temperature can be determined from the absorption data using a similar procedure to the Kranendonk et al. method [19]. Specifically, the Beer-Lambert law is used to determine the amount of intensity that is absorbed as a laser beam passes through a test gas. A reference laser beam is used to correct for absorption by ambient H_2O molecules in the test gas data. These experimental absorption data can then be converted to temperature and H_2O concentration values by fitting them to simulated absorption spectra.

IV. Data Analytics Method

The Peters et al. [17] data analytics method was used in this study to detect precursors to flameout. A brief description of the method is included here and a more detailed account can be found in the original paper by Peters et al. [17]. This method involves first using a time series model to transform the acoustic and absorption data to a white noise process, which is an uncorrelated process with zero mean and constant variance. This step is important because it filters nonstationary behavior and serial correlation from the data that would otherwise cause an unacceptable number of false alarms to be detected. A fault detection algorithm was then used to identify statistical irregularities in the filtered data that increase in frequency as flameout is approached.

An ARIMA(2,1,1)-IGARCH(1,1) time series model is used to filter the data, as detailed below:

$$\begin{gathered}\nabla X_i = \mu + \phi_1 \nabla X_{i-1} + \phi_2 \nabla X_{i-2} + \theta_1 a_{i-1} + a_i \qquad (1) \\ \sigma_i^2 = Var(a_i | a_{i-1}) = \alpha_0 + \alpha_1 a_{i-1}^2 + \eta_1 \sigma_{i-1}^2, \alpha_0 > 0, \alpha_1, \eta_1 \geq 0, \alpha_1 + \eta_1 = 1\end{gathered}$$

The first line in Equation 1 denotes the Autoregressive Integrated Moving Average (ARIMA) portion of the model. In this equation, $\nabla X_i = X_i - X_{i-1}$ is the difference in the absorption temperature data at consecutive sampling intervals (i.e., 1 msec for 1 kHz measurements). Since a single differencing operation is performed on the raw temperature data, the I term is 1. However, the I term is set to zero for the acoustic data because it naturally has zero mean. The AR term refers to the dependence of ∇X_i on the previous two sampling intervals, and the MA term refers to the dependence of ∇X_i on the model residual at samples $i - 1$. The order of the model was selected via the Hyndman-Khandakar algorithm [20]. To account for the increasing signal-to-noise ratio in the data as FO is approached, the conditional variance of the model residuals $a_i, i = 1,2, \ldots$ is modeled using an Integrated Generalized Autoregressive Conditional Heteroscedasticity (IGARCH) process of order (1,1). This algorithm, which is expressed in the second line in Equation 1, is designed to model processes with short bursts of increased variation. By imposing the constraint that the coefficients sum to one, IGARCH can model processes with a trend in the variability.

The data filtering step consists of a training phase and a testing phase. In the training phase, the ARIMA-IGARCH model is fit to training data that were taken at $\dot{V}_{CH4}$=350 SLPM when the flame is stable. The ARIMA-IGARCH parameters (i.e., μ, ϕ_1, ϕ_2, θ_1, α_0, α_1, and η_1 from Equation 1) are then averaged over all 10 training (i.e., $\dot{V}_{CH4}$=350 SLPM) realizations to construct a global time series model. This global model is then used in the testing phase to transform a test case of acoustic or temperature data to a white noise process, which properly prepares it for the fault detection algorithm.

Statistical irregularities in the filtered data were identified using a fault detection algorithm known as an EWRMS control chart. The Exponentially Weighted Root Mean Squared-error (EWRMS) control chart was originally developed by MacGregor and Harris [21] to detect changes in a process' variance. The algorithm converts the filtered data to a series of characteristic values whose quality depends on their magnitude relative to certain control limits. Faults, or "alarms", are instances where the quality characteristic exceeds the control limits. If the control limits are set appropriately, they should not be exceeded by the stable burning cases.

The EWRMS control chart is implemented by first averaging small batches of the filtered test data.

$$\bar{Z}_k = b^{-1} \sum_{i=b(k-1)}^{bk} Z_i \qquad (2)$$

In Equation 2, $\bar{Z}_k$ denotes the average value of the filtered test data in each batch, b is the batch size, and Z_i is the original array of filtered test data. This step helps ensure that the inputs to the EWRMS control chart are normally and independently distributed with zero mean and unit variance, which is an underlying assumption of the algorithm. The quality characteristic at batched index k is computed as follows:

$$S_k = \sqrt{(1-\gamma) S_{k-1}^2 + \gamma \bar{Z}_k^2}, k = 1,2, \ldots, \lceil b^{-1} T_n \rceil \qquad (3)$$

where γ is a constant $(0 < \gamma \leq 1)$ that determines the amount of weight placed on the memory of the quality characteristic and $\lceil\cdot\rceil$ is the round up operator. In this study, $\gamma = 0.2$, $b = 20$, and $\beta = 0.0027$. For a predetermined false alarm rate β, the upper and lower control limits for each individual series of data points are equal to the $100(1 - \beta)$th and 100βth percentiles of the quality characteristic, respectively. The global control limits are then computed by averaging the individual control limits for each of the ten $\dot{V}_{CH4}$=200 SLPM and/or $\dot{V}_{CH4}$=250 SLPM realizations.

V. Results

It is the authors' position that this study presents a much more effective flare monitoring strategy than OGI cameras. It will be shown below that the data analytics method accurately captures the localized flame extinction/re-ignition processes that precede FO and are evidence of a decreased combustion efficiency. Furthermore, FO was easily identifiable in the acoustic and absorption temperature measurements. In contrast, the results that will be discussed in this section raise serious questions about whether OGI cameras can effectively accomplish the flare monitoring objectives of the EPA. Specifically, it was difficult to differentiate hot combustion products from unburned methane emissions in the GFx320 images.

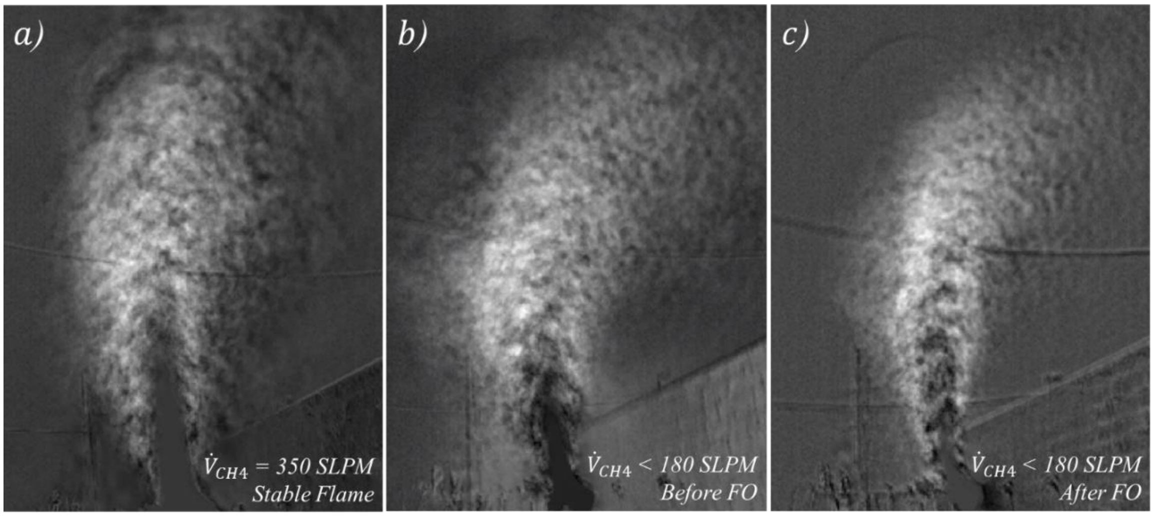

Figure 3: Average GFx320 images at a) $\dot{V}_{CH4}$=350 SLPM and b), c) $\dot{V}_{CH4}$<180 SLPM. Image b) comprises $\dot{V}_{CH4}$<180 SLPM data taken before FO occurred and image c) is from the same test case after FO occurred.

Average images from the GFx320 for a stable burning case ($\dot{V}_{CH4}$=350 SLPM) and a test case where FO occurred during the data recording ($\dot{V}_{CH4}$<180 SLPM) are shown in Figure 3a) and Figure 3b), respectively. The primary differences between these images are the length of the flare plume, the amount of bending that it experiences, and the distinctiveness of the plume boundary. Although inconclusive, the distinctiveness of the plume boundary may be the best available indicator of combustion efficiency. As was discussed previously, hot combustion products create sharp index of refraction gradients that appear much like unburned methane emissions in the OGI camera images. One way to differentiate these two sources of OGI camera signal is to examine their intensity far away from the flare. The index of refraction gradients will fade as the combustion products advect away from the flare and cool, whereas the methane emissions will persist until their concentration drops below a detectable level. A test case with a low combustion efficiency would therefore have higher intensity OGI camera signal far from the flare. Furthermore, a decreased combustion efficiency would blur the boundary between the far field region, where the camera primarily detects unburned methane emissions, and the near-flare region, where the camera also detects undesired signal from sharp index of refraction gradients. Since unburned methane emissions are presumably greater for the $\dot{V}_{CH4}$<180 SLPM case than the $\dot{V}_{CH4}$=350 SLPM case, this may explain why the plume boundary is more clearly defined in Figure 3a) than in Figure 3b). In summary, although some inferences can be made about combustion efficiency from these images, they are largely ambiguous because hot combustion products interfere with the working principles of the camera.

The GFx320 was particularly ineffective at identifying FO occurrences. Figure 3b) and Figure 3c) show two average OGI camera images that were taken by the GFx320 during the $\dot{V}_{CH4}$<180 SLPM test case where FO occurred. Figure 3b) is averaged over all frames before FO and Figure 3c) is averaged over all frames after FO. The primary difference between these average images is that the "trail" of emissions is narrower in Figure 3c) (after FO) than in Figure 3b) (before FO). However, these differences are minor and would be difficult to notice without prior knowledge of which image represents the weakly burning flame (Figure 3b) and the jet of unburned methane (Figure 3c). These subtleties, combined with the high dimensional information of spatially and temporally resolved camera data, present significant challenges to using such data for continuous on-line monitoring of combustion efficiency or FO onset.

The Experimental Setup section describes a test matrix that systematically moved the gas flare test rig from stable burning to FO, with the rig being "parked" at discrete test points along this path. Absorption and acoustic measurements were taken at each of these test points. Figure 4 shows the absorption temperature time series for a stable burning case ($\dot{V}_{CH4}$=350 SLPM) and a near-FO case ($\dot{V}_{CH4}$=180 SLPM). Clear differences can be observed in the mean and variance between these data. The temperature values for the stable burning case have a mean that is approximately 300 K greater than the near-FO case and display regular fluctuations about the mean. Alternatively, the near-FO temperatures exhibit irregular bursts where the temperature values temporarily approach those of a stable flame. It should also be noted that the temperature values in this plot are much lower than typical adiabatic flame temperatures. This is because TDLAS is a path-integrated technique that also includes contributions from cool H_2O molecules that were present along the beam path. Furthermore, Figure 5 shows the average temperature measured by TDLAS for each of the different fuel flow rates. These results have been averaged over each of the 10 realizations corresponding to the different fuel flow rates. On average, the absorption temperature is ~160 K greater at the stable $\dot{V}_{CH4}$=350 SLPM condition than the near-FO $\dot{V}_{CH4}$=180 SLPM condition. However, there is only a ~50 K difference in average temperature between the $\dot{V}_{CH4}$=250 SLPM and $\dot{V}_{CH4}$=350 SLPM cases with a steep decline in the average temperature thereafter.

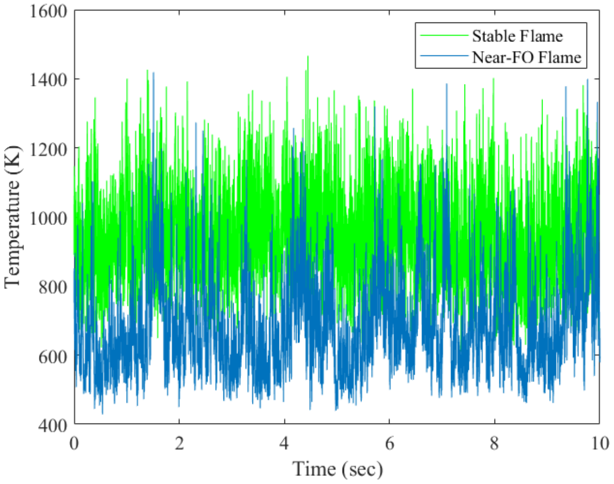

Figure 4: Temperature time series corresponding to a stable burning case ($\dot{V}_{CH4}$=350 SLPM) and a near-FO case ($\dot{V}_{CH4}$=180 SLPM).

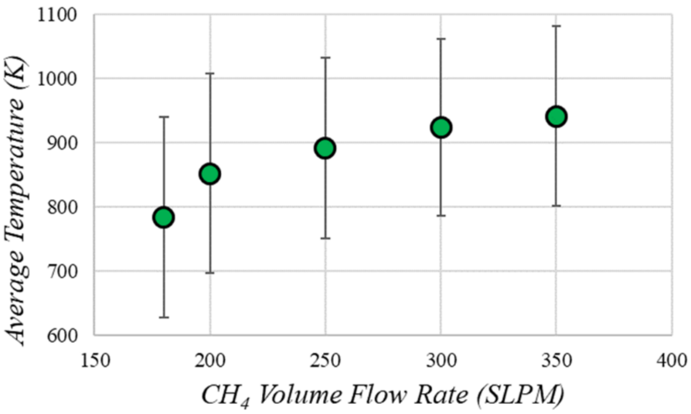

Figure 5: The average temperature as measured by TDLAS shown as a function of the CH_4 volume flow rate.

In contrast to the OGI camera, the acoustic and temperature measurements proved to be very effective for identifying FO. The absorption spectroscopy data is valuable because it provides quantitative temperature measurements at a local region of interest, and the acoustic data effectively "sees" (detects) unsteady flame dynamics throughout the entire flame volume. Furthermore, these kHz rate measurements are able to resolve the FO transient. Figure 6 shows the acoustic and temperature time series corresponding to the FO occurrence test case (i.e., the $\dot{V}_{CH4}<180$ SLPM test case discussed in Figure 3). It is immediately apparent from these time series that FO occurred 48 seconds into the recording. FO can be identified by the sharp change in amplitude in the acoustic data and by the sudden decrease to 400 K temperature values in the absorption data time series.

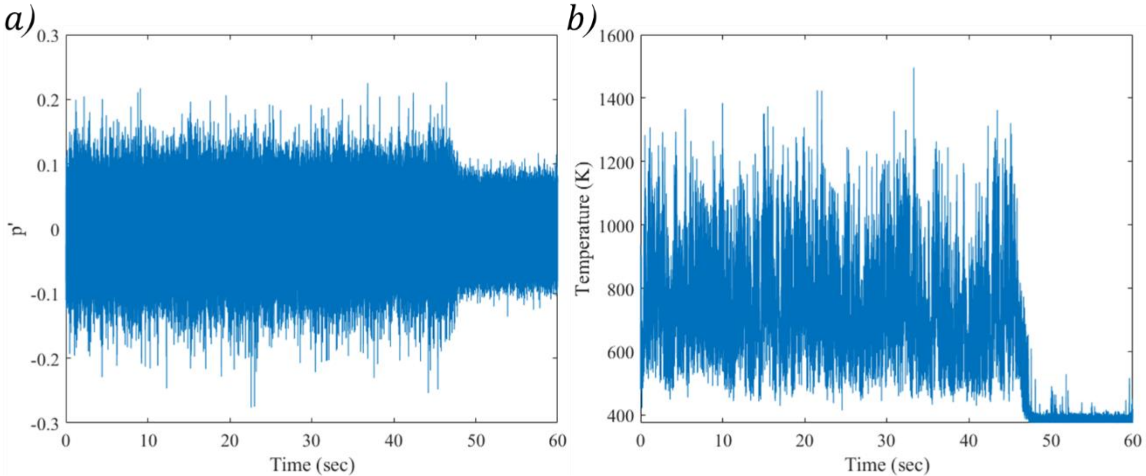

Figure 6: a) acoustic and b) temperature time series from the $\dot{V}_{CH4}<180$ SLPM test case where FO occurred during the data recording.

Combustion inefficiencies were identified in the absorption and acoustic data using the Peters et al. [17] data analytics methodology. Figure 7a) shows outputs from the data analytics method when the absorption temperature data are used as inputs. Results are shown for two individual cases: one stable burning case with $\dot{V}_{CH4}=300$ SLPM and one near-FO case with $\dot{V}_{CH4}=180$ SLPM. The red lines represent control limits, and alarms are identified by magenta symbols in Figure 7. A key takeaway from this plot is that the $\dot{V}_{CH4}=300$ SLPM data never exceeds the control limits, whereas several alarms were activated by the $\dot{V}_{CH4}=180$ SLPM data. This was expected since the flame burned in a stable manner at $\dot{V}_{CH4}=300$ SLPM and it operated on the threshold of flameout at $\dot{V}_{CH4}=180$ SLPM.

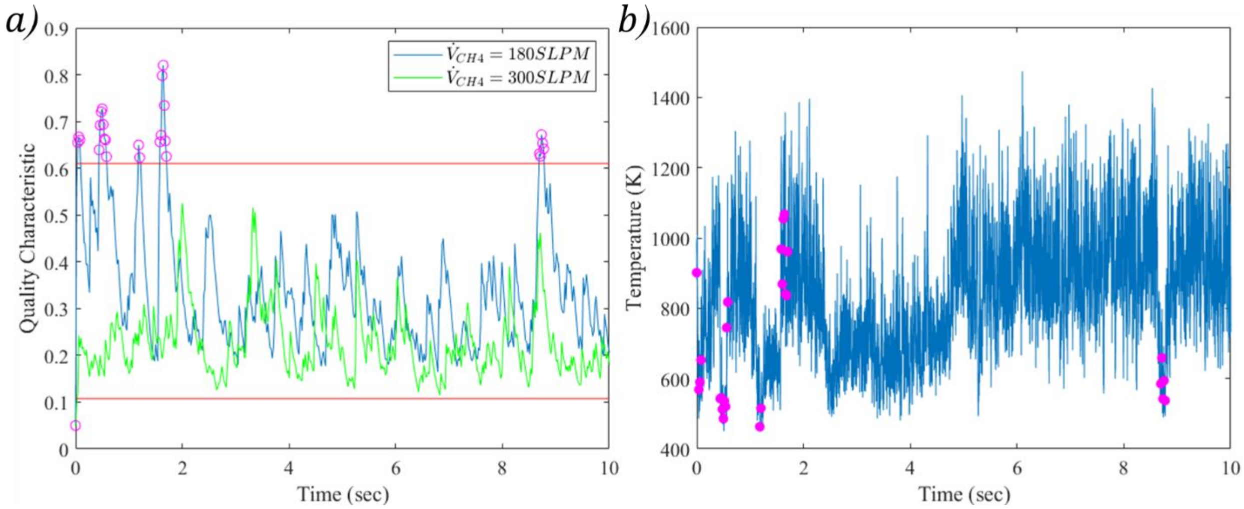

Figure 7: a) control chart based on absorption data from a stable $\dot{V}_{CH4}=300$ SLPM case and a near-FO $\dot{V}_{CH4}=180$ SLPM case. b) The absorption temperature time series corresponding to the $\dot{V}_{CH4}=180$ SLPM case shown in plot a). Alarms are represented by magenta symbols in this figure.

One can appreciate the physical meaning that underlies alarms from the data analytics method by considering where they are situated in the absorption temperature time series. Figure 7b) plots both the absorption temperature time series and the alarms corresponding to the $\dot{V}_{CH4}$=180 SLPM case that was analyzed in Figure 7a). It is clear from Figure 7b) that sudden fluctuations in the temperature time series are required to activate an alarm. These alarms, therefore, likely represent combustion inefficiencies in the form of localized extinction and re-ignition processes, which are known from accepted flame stability theory to precede complete flameout [5]. Two remaining points about the data analytics method should also be noted. First, the method does not differentiate between rapid spikes (re-ignition) and dips (extinction) in the absorption time series data; both will activate alarms. Second, gradual temperature changes were occasionally observed in the $\dot{V}_{CH4}$=180 SLPM data (e.g., between 3-7 seconds in Figure 7b) that did not directly activate alarms. They do, however, indirectly affect the alarm rate because they create conditions where localized extinction/re-ignition occurrences are likely.

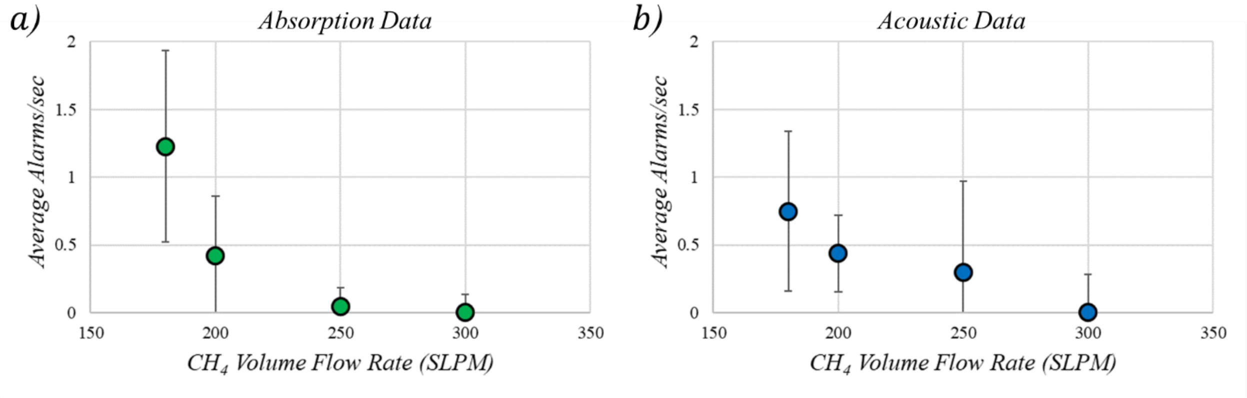

Figure 8: Average number of alarms/second that occurred during the measured a) absorption and b) acoustic time series. Results are shown for the different test cases, which are represented by their CH_4 volume flow rate.

The average number of alarms that were detected by the data analytics method was found to increase as $\dot{V}_{CH4}$ was decreased. Figure 8 plots the average number of alarms/second for each of the various $\dot{V}_{CH4}$ test cases. Results are shown for both the absorption temperature data in Figure 8a) and the acoustic data in Figure 8b). Beginning with the absorption temperature data, alarms were only very rarely activated until $\dot{V}_{CH4}$=200 SLPM. The average alarm rate then increases sharply and peaks at the $\dot{V}_{CH4}$=180 SLPM condition. Similar trends were observed when the data analytics method was applied to the acoustic data. However, the average acoustic alarm rate increases more gradually as $\dot{V}_{CH4}$ is decreased. For example, the average number of alarms/second is only slightly greater at $\dot{V}_{CH4}$=200 SLPM than at $\dot{V}_{CH4}$=250 SLPM. In practice, a high frequency of alarms would notify a flare operator that changes to the combustion system must be made to avoid FO and restore a high combustion efficiency. Furthermore, Figure 8 is valuable for identifying the safety margin above FO where a high combustion efficiency will be maintained and unburned methane emissions avoided.

The physics of the flameout process endow the data analytics methodology that is presented here with a forecasting capability that allows low combustion efficiency operation to be resolved before FO transpires. According to accepted flame stability theory [5], a flame's combustion efficiency will monotonically decrease as it progresses from stable burning to FO. This was demonstrated in Figure 8 where the average number of alarms/second increased monotonically as flameout was approached. Furthermore, Figure 9a) shows the control chart corresponding to the time series data that was presented in Figure 6, which was from the $\dot{V}_{CH4}$<180 SLPM test case where FO occurred during the measurement acquisition process. Results for the absorption temperature data are shown in blue with red control limits and results for the acoustic data are shown in yellow with green control limits. A histogram of the alarm rate is shown in Figure 9b) to illustrate how the alarm rate evolves in time. The following key conclusions can be reached from Figure 9:

1. Clusters of absorption alarms (magenta symbols) tend to appear during time intervals when acoustic alarms (black symbols) are also most densely concentrated. The acoustic alarms are more common, however, as they are activated in many instances when the absorption data is well within the control limits. This demonstrates how both sets of measurements provide complimentary information. The acoustic data effectively "sees" (detects) unsteady flame dynamics throughout the entire flame volume whereas the absorption measurements provide quantitative temperature data at a local region of interest.

2. Both the acoustic and absorption alarms increase in frequency as FO is approached. This is consistent with the results that were shown in Figure 8 and expectations from flame stability theory of decreased combustion efficiency as FO is approached. These results provide further evidence that the alarms actually represent localized flame extinction/re-ignition processes and thereby signal when FO is imminent.
3. Flameout occurs 3-4 seconds after the alarms reach their peak frequency. This is a more gradual process than what was observed in the authors previous work [17] on swirl-stabilized spray flames. In this previous study, the flame globally extinguished almost immediately after the alarm frequency peaked.

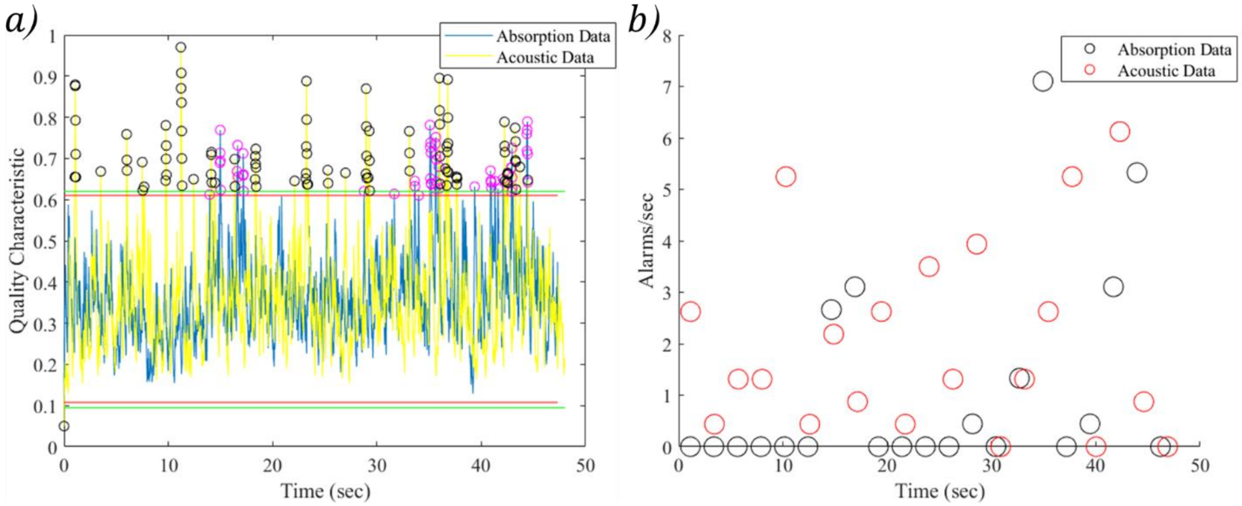

Figure 9: a) control chart based on both absorption and acoustic data from the $\dot{V}_{CH4}$<180 SLPM test case where FO occurred during the data recording. b) Histogram of the alarm rate as a function of time for both data types.

VI. Conclusions

The primary objective of this study was to apply a data analytics methodology to experimental temperature and acoustics measurements for the purpose of maintaining a high combustion efficiency in gas flares. The experimental data were acquired in a representative gas flare test rig that was developed at Georgia Tech based on a Zeeco manufactured air-assisted flare tip. The test matrix included stable burning data, data acquired when the flame operated on the threshold of flaming out, and intermediate conditions between these extremes. Data were also acquired from a test case where the FO process occurred during the experiment, which allowed the transient effects of this phenomenon to be captured. An EPA certified optical gas imaging (OGI) camera was used to visualize the flame and observe unburned methane emissions during the measurements. Although some inferences could be made about combustion efficiency from these images, they were largely ambiguous as hot combustion products interfered with the working principles of the camera. On the other hand, the data analytics method clearly identified local flame extinction/re-ignition processes from kHz rate acoustic and absorption spectroscopy data. These localized extinction/re-ignition processes were found to monotonically increase in frequency as flameout was approached. The data analytics method was therefore shown to be a powerful tool for predicting flameout and identifying operational regimes where a gas flare will maintain a high combustion efficiency. Taken together with the authors' previous work [17] on swirl-stabilized spray flames, these results demonstrate that the data analytics method presented here is an effective combustion efficiency monitoring tool that is generalizable across a variety of different combustion systems (e.g., premixed, nonpremixed, or liquid-fueled), combustor geometries, or operating conditions.

Acknowledgments

This material is based upon work supported by the U.S. Department of Energy, Office of Science, Office of Fossil Energy and Carbon Management, under Award Number DE-SC0023746.

References

[1] T. Hodges and J. Potter, "Transportation's Role in Reducing US Greenhouse Gas Emissions: Volume 1: Synthesis Report and Volume 2: Technical Report," 2010.

[2] O. Boucher, P. Friedlingstein, B. Collins, and K. P. Shine, "The indirect global warming potential and global temperature change potential due to methane oxidation," *Environmental Research Letters*, vol. 4, no. 4, p. 044007, 2009.

[3] U. S. EPA, "EPA's Final Rule for Oil and Natural Gas Operations Will Sharply Reduce Methane and Other Harmful Pollution," 2023. [Online]. Available: https://www.epa.gov/controlling-air-pollution-oil-and-natural-gas-operations/epas-final-rule-oil-and-natural-gas.

[4] D. R. Lyon *et al.*, "Concurrent variation in oil and gas methane emissions and oil price during the COVID-19 pandemic," *Atmospheric Chemistry and Physics*, vol. 21, no. 9, 2021.

[5] S. Shanbhogue, S. Husain, and T. Lieuwen, "Lean blowoff of bluff body stabilized flames: Scaling and dynamics," *Progress in Energy and Combustion Science*, vol. 35, no. 1, pp. 98–120, 2009.

[6] S. Nair and T. Lieuwen, "Near-blowoff dynamics of a bluff-body stabilized flame," *Journal of Propulsion and Power*, vol. 23, no. 2, pp. 421–427, 2007.

[7] R. Erickson and M. Soteriou, "The influence of reactant temperature on the dynamics of bluff body stabilized premixed flames," *Combustion and Flame*, vol. 158, no. 12, pp. 2441–2457, 2011.

[8] B. Emerson, J. O'Connor, M. Juniper, and T. Lieuwen, "Density ratio effects on reacting bluff-body flow field characteristics," *Journal of Fluid Mechanics*, vol. 706, pp. 219–250, 2012.

[9] J. A. Sutton and J. F. Driscoll, "Imaging of local flame extinction due to the interaction of scalar dissipation layers and the stoichiometric contour in turbulent non-premixed flames," *Proceedings of the Combustion Institute*, vol. 31, no. 1, pp. 1487–1495, 2007.

[10] M. Juddoo and A. Masri, "High-speed OH-PLIF imaging of extinction and re-ignition in non-premixed flames with various levels of oxygenation," *Combustion and Flame*, vol. 158, no. 5, pp. 902–914, 2011.

[11] A. M. Steinberg, I. Boxx, C. M. Arndt, J. H. Frank, and W. Meier, "Experimental study of flame-hole reignition mechanisms in a turbulent non-premixed jet flame using sustained multi-kHz PIV and crossed-plane OH PLIF," *Proceedings of the Combustion Institute*, vol. 33, pp. 1663–1672, 2011.

[12] T. M. Muruganandam, "Sensing and Dynamics of Lean Blowout in a Swirl Dump Combustor," Georgia Institute of Technology, 2006.

[13] S. Nair and T. Lieuwen, "Acoustic detection of blowout in premixed flames," *Journal of Propulsion and Power*, vol. 21, no. 1, pp. 32–39, 2005.

[14] T. Yi and E. Gutmark, "Real-time prediction of incipient lean blowout in gas turbine combustors," *AIAA Journal*, vol. 45, no. 7, 2007.

[15] V. Unni and R. I. Sujith, "Precursors to blowout in a turbulent combustor based on recurrence quantification," in *52nd AIAA/SAE/ASEE Joint Propulsion Conference*, 2016.

[16] S. Mondal, S. De, A. Mukhopadhyay, S. Sen, and A. Ray, "Early prediction of lean blowout from chemiluminescence time series data," *Combustion Science and Technology*, vol. 194, no. 6, 2022.

[17] B. Peters, N. Rock, B. Emerson, N. Gebraeel, and K. Paynabar, "Data Analytics Method for Detecting Extinction Precursors to Lean Blowout in Spray Flames," *Combustion Science and Technology*, vol. 194, no. 13, pp. 2597–2612, 2022.

[18] R. Rajaram and T. Lieuwen, "Acoustic radiation from turbulent premixed flames," *Journal of Fluid Mechanics*, vol. 637, pp. 357–385, 2009.

[19] L. A. Kranendonk, A. W. Caswell, and S. T. Sanders, "Robust method for calculating temperature, pressure, and absorber mole fraction from broadband spectra," *Applied Optics*, vol. 46, no. 19, 2007.

[20] R. J. Hyndman and Y. Khandakar, "Automatic Time Series Forecasting: The forecast Package for R," *Journal of Statistical Software*, vol. 27, no. 3, 2008.

[21] J. F. MacGregor and T. J. Harris, "The exponentially weighted moving variance," *Journal of Quality Technology*, vol. 25, no. 2, 1993.